Development and Relaxation of Stress in Surface Layers; Composition and Residual Stress Profiles in γ'-Fe_4N_{1-x} Layers on α-Fe Substrates

M.A.J. SOMERS and E.J. MITTEMEIJER

Composition-depth and (residual) stress-depth profiles were investigated in two different γ'-Fe_4N_{1-x} surface layers on α-iron substrates. X-ray diffraction analysis was applied. Determination of the actual lattice-spacing depth profiles required correction for the effect of penetration of the X-rays. The dependence of the nitrogen content in γ'-Fe_4N_{1-x} surface layers on depth below the surface corresponds with that expected for diffusion-controlled layer growth. The formation of porous grain boundaries (channels) in the surface-adjacent part of the layers provides the possibility of nitrogen uptake at "internal" surfaces during nitriding, leading to the development of concave concentration-depth profiles in this part of the layers. Stress buildup in the massive interface-adjacent part of γ'-Fe_4N_{1-x} layers on α-Fe substrates originates from both the presence of a concentration-depth gradient and the difference in thermal contraction between layer and substrate on cooling from the nitriding temperature to the measurement temperature. Channel/pore development along grain boundaries in the surface-adjacent part of the layers provides a mechanism for stress relaxation during nitriding. On cooling, the channels can also accommodate part of the thermally induced misfit. Lateral strain gradients in the most severely porous part of the layers are revealed by the X-ray diffraction analysis.

I. INTRODUCTION

IMPROVEMENT of surface-quality dependent properties of workpieces, such as the resistance against corrosion and wear, is frequently established by the application of surface layers. Generally, surface layers are both chemically and physically distinct from the underlying substrates.

Residual (internal) stresses occur when the tendency of separate portions of a specimen to assume different volumes is counteracted by cohesive forces. By their nature, residual stresses persist in the absence of an external load. Residual stresses can be either beneficial or detrimental for the service life of workpieces.[1]

Nitriding and nitrocarburizing are widely applied thermochemical surface treatments for the improvement of wear, corrosion, and fatigue properties of (usually ferritic) steels.[2] On nitriding (nitrocarburizing), nitrogen (nitrogen and carbon) is (are) offered to a steel surface at a temperature below 863 K (*cf.* Fe-N phase diagram[3]). The case produced can be subdivided into a compound layer, consisting predominantly of iron (carbo)nitrides (ε-$Fe_2(N,C)_{1-x}$ and γ'-$Fe_4(N,C)_{1-x}$) and a diffusion zone, containing, at the treatment temperature, interstitially dissolved nitrogen and, possibly, a dispersion of alloying-element nitrides.

Until now, no systematic investigation of the coexisting (residual) stress and composition profiles within the compound layer has been performed. The few data published so far[4,5] concern residual stresses in *dual-phase* ε/γ' compound layers produced by *commercial* treatments, which hinder straightforward interpretation of the results obtained. As a first step in a research project on compound-layer formation (see also Reference 6), the present paper deals with the determination and interpretation of residual stresses in γ'-Fe_4N_{1-x} layers produced on α-Fe substrates by gaseous nitriding. As will be shown, this layer/substrate system can be considered as a model for stress development (in surface layers) resulting from simultaneously occurring compositional and thermal misfits.

Lattice spacings of crystalline material depend on the state of stress and the composition. Hence, diffraction methods can be utilized for the determination of stress and composition. In this work, the established $\sin^2\psi$ (X-ray) diffraction method for stress analysis will be employed. However, if both stress and compositional variations occur within the material to be analyzed, the extraction of both a value for the stress and a value for the composition from the (X-ray) diffraction data can only be achieved after appropriate unraveling of the various contributions to the signal recorded. The method employed in this paper is discussed in Section II.

II. DETERMINATION OF MACROSTRESS- AND COMPOSITION-DEPTH PROFILES BY DIFFRACTION METHODS

A general discussion on the diffraction method for macrostress determination in a triaxial state of stress has been given in References 7 and 8. X-ray diffraction methods for the analysis of macro- and microstresses in polycrystalline surface layers have been reviewed recently in Reference 9. For massive polycrystalline surface layers, a state of plane stress with equal principal stresses, σ_{11} and σ_{22} ($\sigma_{//} \equiv \sigma_{11} = \sigma_{22}$; Figure 1), can usually be assumed, because

M.A.J. SOMERS, formerly Graduate Student, Laboratory of Metallurgy, Delft University of Technology, is with Philips, Eindhoven, The Netherlands. E.J. MITTEMEIJER, Professor, is with the Laboratory of Metallurgy, Delft University of Technology, Rotterdamseweg 137, 2628 AL Delft, The Netherlands.

Manuscript submitted February 23, 1989.

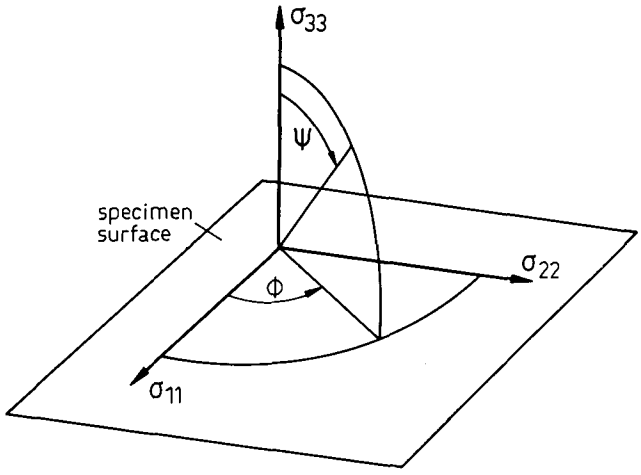

Fig. 1—Definition of Euler angles ψ and ϕ with respect to the overall state of stress.

(1) the relative misfit between the equilibrium dimensions of the surface layer and the substrate and the effective elastic constants do not depend on ϕ (Figure 1), and
(2) the specimen edge effects can be ignored for the surface area irradiated in the experiment.

Rotation of the specimen around its surface normal always allows stress analysis in terms of $\sigma_{//} = (\sigma_{11} + \sigma_{22})/2$.*

*σ_{11} will be unequal to σ_{22} only for an elastically anisotropic surface layer in conjunction with the presence of preferred orientation not involving a fiber texture with fiber axis perpendicular to the surface.

Then it holds for the lattice spacing, d_ψ, measured in a direction characterized by the angle ψ made with the specimen surface normal (Figure 1), that

$$d_\psi = d_0 + 2S_1 d_0 \sigma_{//} + \frac{1}{2} S_2 d_0 \sigma_{//} \sin^2 \psi \qquad [1]$$

where d_0 is the strain-free, reference lattice spacing and S_1 and $(1/2)S_2$ denote the so-called X-ray elastic constants. According to Eq. [1], plotting of d_ψ *vs* $\sin^2 \psi$ yields a straight line; a value for $\sigma_{//}$ follows from its slope, or the intercept with the ordinate at $\psi = 0$, provided d_0 and $(1/2)S_2$ or S_1 are known.

In order to find a reliable value for $\sigma_{//}$, d_0 does not need to be known precisely; in general, $d_{\psi=0}$ will not deviate more than about 1 pct from d_0 and an accurate value for $\sigma_{//}$ is obtained by replacing d_0 by the experimental $d_{\psi=0}$ in the expression for, *e.g.*, the slope. On the other hand, a precise value for the strain-free spacing, d_0, is required if the occurring composition of the diffracting material has to be determined. The experiment provides a route to determine the strain-free lattice spacing. It follows from Eq. [1] that $d_\psi = d_0$ if $\psi = \psi_0$, where ψ_0 indicates the "strain-free direction," which obeys[9,10]

$$\sin^2 \psi_0 = \frac{-2S_1}{\frac{1}{2} S_2} \qquad [2]$$

Thus, interpolation in a $(d_\psi, \sin^2 \psi)$ graph provides a value for d_0.

Consider a stress-free surface layer containing a composition-depth profile. Such a profile can be traced by (X-ray) diffraction determinations of the lattice spacing after successive removal of sublayers. The presence of a state of (plane) stress generally influences the value of the lattice parameter (*cf.* Eq. [1]). But as long as $\sigma_{11} = \sigma_{22}$ and $\sigma_{33} = 0$, the strain-free direction (Eq. [2]) does not depend on the value of the stress, assuming a negligible dependence of the ratio $S_1/(1/2)S_2$ on composition and stress. This leads to an important result: even in the presence of depth-dependent stresses, a composition-depth profile can be traced unambiguously by determination of the strain-free lattice spacing, according to Eq. [2], after each removal of a sublayer.

The determination of stress- and composition-depth profiles can be based on X-ray diffraction analysis at different depths by removal of sublayers, provided that the X-ray penetration in the material to be analyzed is significantly smaller than the extent of the depth profiles. Each spacing determined represents some diffracting-volume weighted average, and a correction should normally be made.

Assuming the lattice spacing as derived from the peak or centroid position of an X-ray diffraction line profile to be intensity-weighted, the value obtained for the lattice spacing, $\langle d \rangle$, determined for a surface layer of thickness, t, can be expressed as[9,10,11]

$$\langle d \rangle = \frac{\int_0^t d(z) \cdot \exp[-\mu k z] \cdot dz}{\int_0^t \exp[-\mu k z] \cdot dz} \qquad [3]$$

where z denotes the depth below the actual surface, $d(z)$ indicates the actual lattice spacing, μ is the linear absorption coefficient, and k is a diffraction-geometry dependent factor (Appendix A). Because k depends on the tilt angle,* a stress-free surface layer containing a concentration-depth profile could be misinterpreted as internally stressed if the $\sin^2 \psi$ method would be employed without more ado. Such fictitious or ghost stresses can attain a considerable magnitude, as illustrated in Appendix A for the case of both stress-free and stressed γ'-Fe_4N_{1-x} layers containing a concentration-depth profile.

*Using a ψ goniometer, tilt angle = ψ. Using an ω goniometer, tilt angle = ω; then, ω takes the role of ψ in Eqs. [1] and [2].

Procedures to avoid ghost-stress effects during data evaluation have been proposed.[7–9,11–16] For example, it has been suggested[8,10–12] that a value for the slope of a $(\langle d \rangle, \sin^2 \psi)$ plot could be conceived as intensity-weighted in the sense of Eq. [3], with application of some average value for k. However, considerable variation of k can occur as ψ changes and, consequently, a ghost-stress affected stress value will be obtained. An analogous objection holds for such a correction method applied to the intensity-weighted strain.[7,15] In fact, on the basis of Eq. [3], each data point of the $(\langle d \rangle, \sin^2 \psi)$ plot has to be corrected for penetration of X-rays.

From X-ray diffraction analysis after each sublayer removal, the diffracting-volume weighted Bragg angle, $\langle \theta \rangle$, and thus lattice spacing, $\langle d \rangle$, can be determined as a

function of ψ at different depths in the layer. Then, for each value of ψ, a plot of $\langle d \rangle$ (or $\langle \theta \rangle$) *vs* depth below the original surface can be constructed. Next, each of these curves can be corrected for the effect of penetration of X-rays. Finally, (1) the composition-depth profile is obtained from the corrected lattice-spacing depth profile for $\psi = \psi_0$ and (2) the stress-depth profile follows by straightforward application of Eq. [1] at specified depths below the original surface, using the corrected lattice-spacing data.

For correction of a curve of lattice spacing *vs* depth below the original surface (with ψ = constant), one can proceed in two distinct ways (also see Figure 2):

(1) the spacing measured is assigned to a certain depth below the surface of the specimen actually occurring at the time of the X-ray diffraction measurement. This depth can be prescribed by one of the possible parameters defined to characterize the effect of penetration of the X-rays;[9] the so-called "information depth" appears appropriate (also see Reference 16).

(2) the spacing *at* the surface actually occurring at the time of the X-ray diffraction experiment is calculated from the measured one.

It can be shown that both methods only give identical results if the real spacing depends linearly on depth.[16] Differences between the two methods can usually be ignored if such linearity exists up to the information depth.

For the determination of a stress value at a specific depth below the original surface corrected according to method (1), interpolation is necessarily required in a series of plots of lattice spacing *vs* depth (one plot for each value of ψ; *cf.* Eq. [1]), whereas a direct determination (*i.e.*, a direct application of Eq. [1]) is possible if the measured lattice spacings are corrected according to method (2). This essential difference between methods (1) and (2) can become of importance if a significant change of the value for the stresses results from sublayer removal (*cf.* Appendix C). Therefore, method (2) is preferred in the present paper; it is described in Appendix B.

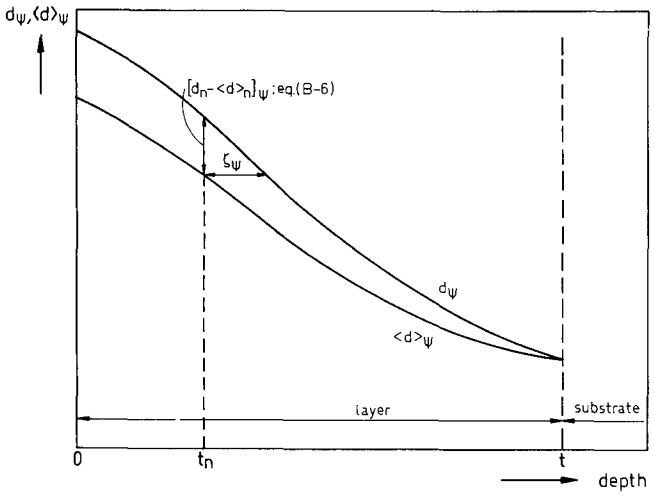

Fig. 2—Correction of the lattice-spacing depth profiles determined, $\langle d \rangle_\psi$, for penetration of the X-rays can be performed by (1) assigning the value for $\langle d \rangle_\psi$ to an information depth, ζ_ψ, below the occurring surface or by (2) calculating the actual value for d_ψ at the occurring surface from the course of the as-determined $\langle d \rangle_\psi$ profile.

III. EXPERIMENTAL

A. *Specimen Preparation*

Specimens in the form of discs (20-mm diameter and 2-mm thickness) were prepared from pure iron (Ferrovac E: 0.005 wt pct C, 0.0003 wt pct N, 0.01 wt pct O, <0.04 wt pct (Cr + Al + Mo + Cu + W)). Before nitriding, the discs were annealed for 1 hour at 923 K in argon. Nitriding was performed at (843 ± 1) K in a vertical quartz-tube furnace. The apparatus used for the nitriding treatments has been described in previous papers.[6] Compositions of the nitriding gas atmosphere and the nitriding times were chosen such that two different layers were obtained on top of the ferrite substrate, *viz.*, a γ' layer practically without porosity visible by optical microscopy* (30 vol pct NH_3/70 vol pct H_2; nitriding time of 15 hours; further denoted as specimen A) and a γ' surface layer with pronounced grain-boundary porosity* (40 vol pct NH_3/60 vol pct H_2; nitriding time of 30 hours; further denoted as specimen B). After nitriding, the specimens were cooled moderately fast by pulling them into a cold chamber of the nitriding apparatus, thus allowing precipitation of γ'-Fe_4N and α''-$Fe_{16}N_2$ in the nitrogen-containing substrate during cooling.

*The occurrence of porosity is inherent to the metastability of iron-nitrogen phases with respect to molecular nitrogen at normal pressures (see Section V).

B. *Metallography*

Optical microscopic analysis of the nitrided specimens was performed applying Neophot 2 and 30 microscopes (Zeiss, Jena). Both cross and oblique sections[6] were examined. The corresponding specimens were mounted in BAKELITE* (at $T \approx 423$ K), ground, polished (0.25-μm diamond paste), and etched for approximately 20 seconds in 1 pct Nital containing 0.1 vol pct concentrated hydrochloric acid.

*BAKELITE is a trademark of Union Carbide Corporation, Danbury, CT.

Average thicknesses of the total γ' layers were determined from layer-thickness measurements (in cross sections at 500 times magnification) along 50 equidistant lines perpendicular to the specimen surface, using a LEITZ DURIMET* microhardness tester.

*LEITZ DURIMET is a trademark of Leitz, Inc.

X-ray diffractometry as described below was performed at different depths within the γ' layers. To this end, very thin sublayers of the γ' layers were removed successively by very careful mechanical polishing treatments (3 → 1 → 0.25-μm diamond paste). The average sublayer thickness removed between successive X-ray diffraction experiments amounts to approximately 1.5 μm.

C. *X-Ray Diffractometry*

X-ray diffraction analysis was performed with a SIEMENS* ω diffractometer (type F) equipped with a

*SIEMENS is a trademark of The Retton and Crane Company.

Co tube and a graphite monochromator in the diffracted beam to select Co K_β radiation. Co K_β is preferred for a minimization of ghost-stress effects in the diffraction analysis of macrostresses in γ'-Fe_4N_{1-x} surface layers containing composition- and stress-depth profiles simultaneously (Appendix A). Utilizing ω goniometers for stress evaluation according to the $\sin^2 \psi$ method (*cf.* Eq. [1]), high diffraction angles (2θ) are required to allow a large ψ ($=\omega$) range. Therefore, the $\{420\}_{\gamma'}$ reflection ($2\theta \cong 145$ deg; Miller indices refer to the fcc sublattice of iron atoms[17]) was chosen. Diffractometer settings are gathered in Table I.

The width of the incident beam divergence slit corresponds with a maximum width of the area irradiated on the specimen surface of 3.0 mm for $\sin^2 \psi = 0.6$. Hence, specimen rotation around its surface normal implies that the fraction of the specimen surface contributing to the diffracted intensity is much smaller than the total specimen surface area (diameter 20 mm). No indication for the presence of preferred orientation was obtained. In view of the rotation symmetry of the occurring stresses within the plane of the specimen ($\sigma_{11} = \sigma_{22}$; see Section II), specimen rotation can be performed to enhance crystal statistics. Counting times were chosen with reference to the total remaining layer thickness after sublayer removals, such that the net number of counts measured at the peak maximum usually equaled about 2500 and that a full number of specimen rotations occurred in a single intensity measurement. X-ray diffraction line profiles (*i.e.*, diffracted intensity as a function of 2θ) were recorded at five equidistant $\sin^2 \psi$ values in the range of 0 to 0.6.

After measurement, each intensity value was corrected for the dead time of the entire system, *i.e.*, 3.5 μs. Background intensity was estimated by fitting a straight line (least-squares analysis) through the first and last 20 data points of each line profile, and it was subtracted accordingly. Further, each intensity value was divided by the appropriate Lorentz-polarization factor.[18] The peak position of the remaining line profile thus corrected was determined by fitting a parabola (least-squares analysis) through those intensities larger than 70 pct of the maximum intensity of the profile. For line profiles obtained near the layer/substrate interfaces, the parabola mentioned was fitted through those intensities larger than 50 pct of the maximum one, in order to increase the amount of intensity data contributing to peak position determination in view of the relatively small diffracted intensities. Finally, the lattice spacings corresponding to the peak positions were calculated. The strain-free lattice spacing (*cf.* Section II) was corrected for the difference between the measurement and the reference temperature; the data given in this paper apply to 293 K (for the linear expansion coefficient of γ'-Fe_4N_{1-x}, see Reference 19).

Table I. Diffractometer Settings Used for X-Ray Stress Analysis

X-ray tube operated at (kV/mA)	45/22
Divergence slit (deg)	0.781
Receiving slit (deg 2θ)	0.137
Diffractometer radius (mm)	186.5
2θ range (deg 2θ)	142 to 149
Stepsize $\Delta 2\theta$ (deg 2θ)	0.06
Counting time (s)	56 to 224
ϕ rotation (rev./min)	1.75
$\sin^2 \psi$ range	0 to 0.6

IV. MAIN RESULTS

Cross sections of the layers produced on nitriding are shown in Figures 3(a) and (b). Average total layer thicknesses, t, together with the depth up to which grain-boundary porosity could be observed in cross sections, t_p, are given in Table II. No porosity was observed by

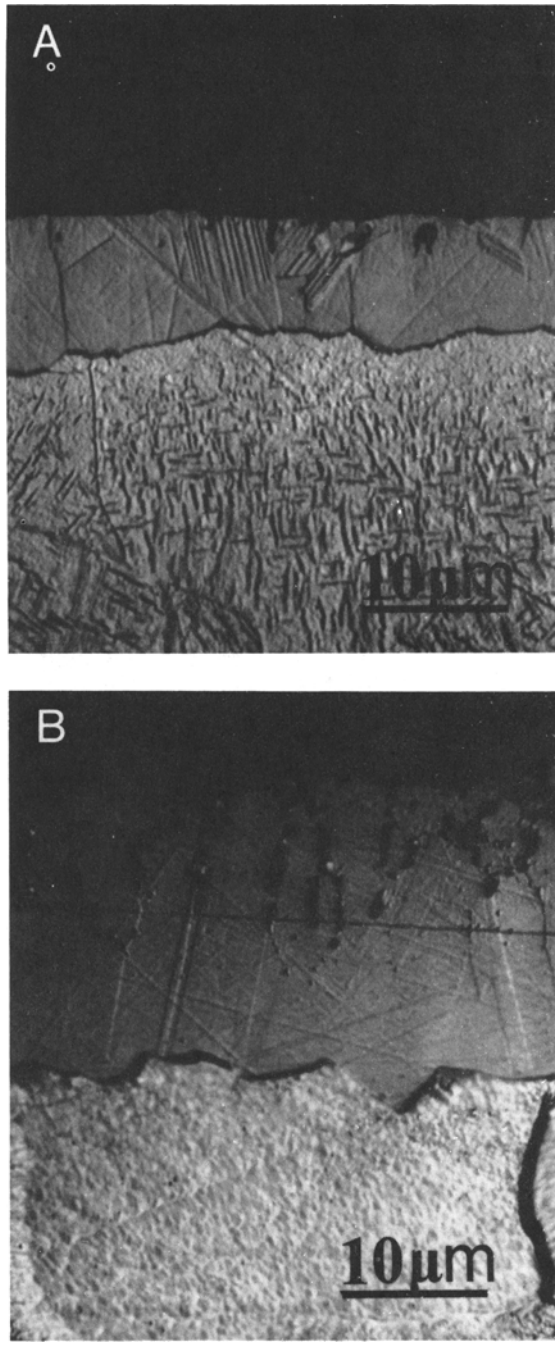

Fig. 3—Optical micrographs (oblique illumination; oil immersion; λ = 480 nm) of cross sections of layers (*a*) A and (*b*) B. Sections were etched in 1 pct Nital + 0.1 vol pct HCl.

Table II. Compound Layer Thickness (t) and Channel Depth (t_p)

Specimen	t (μm)	t_p (μm)
A*	9.3 ± 0.4	≈3
B**	20.6 ± 1.0	10.0 ± 0.4

The 95 pct confidence interval has been indicated, except for t_p of layer A (see text).
*Nitrided in 30 vol pct NH_3/70 vol pct H_2 for 15 h.
**Nitrided in 40 vol pct NH_3/60 vol pct H_2 for 30 h.

optical microscopy within a cross section of the γ' layer of specimen A. However, examination of an oblique section of this layer showed that some porosity is present along grain boundaries in γ' up to about 3 μm below the surface.

Because of the ragged nature of the interfaces between γ' layers and substrates (Figure 3), diffracted intensities of $\{420\}_{\gamma'}$ could be measured at both sides of the average interface positions (Table II) indicated in the figures. The stresses presented at the average interface positions are taken as corresponding averages obtained by interpolation. The value observed for the strain-free lattice spacing in the region beyond the average interface position is constant within experimental error. The ragged quality of the interfaces hinders a straightforward calculation of the linear absorption coefficient, μ, from the decrease in diffracted intensity on successive sublayer removal. Therefore, the value for μ, necessary for application of the correction procedure for the effect of penetration of the X-rays, was taken as the Fe_4N composition-weighted sum of the linear absorption coefficients of Fe and N for Co K_β radiation;[20] *i.e.*, $\mu = 2.349 \times 10^5\ m^{-1}$.

Lattice spacings determined (at $T = 293$ K), $\langle d \rangle$, were corrected for the penetration of X-rays according to Eq. [B6], leading to (corrected) lattice spacing, d, *vs* depth profiles for each direction of ψ employed (Section II). In all cases, the derivative of $\langle d \rangle$ with respect to z in Eq. [B6] was assessed by differentiating a third-order polynomial fit (least-squares analysis) through five successive $(\langle d \rangle_n, t_n)$ data for one particular ψ, where, as far as possible, the depth range for fitting was taken as $[t_{n-2}, t_{n+2}]$.

X-ray elastic constants of γ'-Fe_4N_{1-x} are not known. Because of the crystallographic similarity of γ' (fcc sublattice of iron atoms) and austenite (fcc iron), the X-ray elastic constants were calculated from the single-crystal elastic constants of an austenitic Fe-12 pct Cr-12 pct Ni alloy,[21,22] applying the Kröner-Eshelby model for grain interaction,[23] leading to

$$S_1 = (-2.35 + 3.73\Gamma) \times 10^{-6}\ \text{MPa}^{-1}$$

$$\frac{1}{2} S_2 = (8.38 - 11.2\Gamma) \times 10^{-6}\ \text{MPa}^{-1}$$

where

$$\Gamma = \frac{h^2k^2 + k^2l^2 + l^2h^2}{(h^2 + k^2 + l^2)^2}$$

and h, k, and l are Miller indices with respect to the (fcc) sublattice of iron atoms. (The effect of the presence of Ni and Cr in this alloy on the elastic constants has been shown to be negligible.[22])

Typical examples of $(d_\psi, \sin^2 \psi)$ plots, obtained for different depths below the surface, are shown for layers A and B in Figures 4(a) and (b), respectively. In general, the dependence of d_ψ on $\sin^2 \psi$ can be described very well by a straight line (*cf.* Eq. [1]). Only for the surface-adjacent region (first 5 μm below the outer surface) of layer B, where pronounced porosity occurs, some curvature is observed in the $(d_\psi, \sin^2 \psi)$ plot (the worst case, *i.e.*, *at* the surface, is presented in Figure 4(b)), suggesting that the presupposition of a state of plane stress is not valid. For this particular case, the maximum deviation of individual d_ψ data from a straight line fitted by least-squares analysis to the $(d_\psi, \sin^2 \psi)$ data amounts to 8×10^{-6} nm, which is larger than the experimental error of 3×10^{-6} nm in $\langle d \rangle_\psi$, assessed as corresponding to one-fifth of the stepsize of 0.06 deg 2θ (see Table I) (further discussion in Section VI–C).

The strain parallel to the surface might be obtained from the lattice spacing at $\psi = \pi/2$, as obtained by extrapolation of the $(d_\psi, \sin^2 \psi)$ plot to $\sin^2 \psi = 1$ and the strain-free lattice spacing. However, this strain in fact is an average for only those grains with $\{hkl\}$ perpendicular to the surface. The "overall" macrostrain parallel to the surface, $\varepsilon_{//}$, which represents an average over all grains, is obtained from[9]

$$\varepsilon_{//} = \frac{1 - \nu}{E} \sigma_{//} \qquad [4]$$

where Poisson's constant, ν, and Young's modulus, E, are the "overall" elastic constants and $\sigma_{//}$ follows from the $(d_\psi, \sin^2 \psi)$ plot determined for the reflection considered. The macroscopic elastic constants (E, ν) were calculated from single-crystal elastic constants given for an austenitic iron alloy, using the Kröner-Eshelby grain interaction model (see above): $E = 200.4$ GPa and $\nu = 0.32$.

The resulting stress- and strain-depth profiles are shown in Figures 5(a) and (b). The experimental error in $\sigma_{//}$, due to the experimental error in $\langle d \rangle_\psi$, amounts to $\Delta\sigma_{//} = 17$ MPa (*i.e.*, $\Delta\varepsilon_{//} = 6 \times 10^{-5}$). For the present case, systematic errors in $\sigma_{//}$ and $\varepsilon_{//}$ introduced as a consequence of stress relaxation occurring on sublayer removal can be neglected (Appendix C).

Strain-free lattice parameters, as obtained from interpolation for the strain-free direction ($\sin^2 \psi_0 = 0.497$; *cf.* Eq. [2]) in $(d_\psi, \sin^2 \psi)$ plots, can be directly related to the composition of the γ' phase. Using the lattice-parameter composition dependence provided in Reference 19 (valid for lattice spacings at the reference temperature of 293 K (Section III–C)), the composition-depth profiles shown in Figures 6(a) and (b) were obtained.

V. COMPOSITION OF γ'-Fe_4N_{1-x} SURFACE LAYERS

The nitrogen concentration in the γ' layers decreases with increasing distance away from the external surface (Figures 6(a) and (b)), as would be expected for compound-layer growth controlled by nitrogen diffusion through the layer. The nitrogen content at the surface of a γ' layer can be predicted using recent equilibrium data

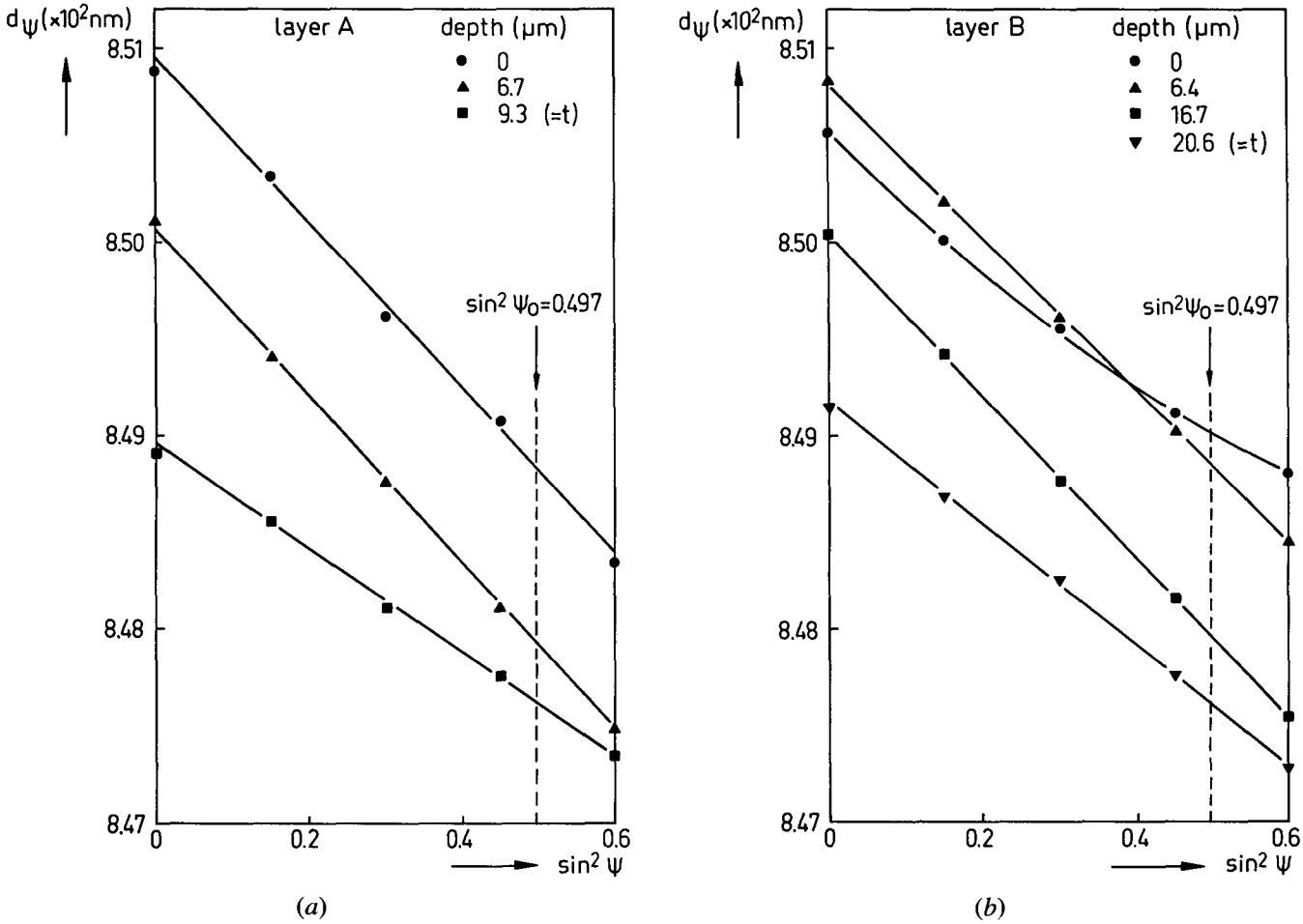

Fig. 4—Dependence of the lattice spacing of $\{420\}_{\gamma'}$, d_ψ, on the tilt angle, ψ, for different total removed sublayer thicknesses for layers (*a*) A and (*b*) B. All data were corrected for the penetration of X-rays. The strain-free direction, $\sin^2 \psi_0$, has been indicated.

for nitrogen absorption in γ' foils (Langmuir absorption isotherms given in Reference 24 and verified in Reference 19). The nitrogen content in a γ' layer at the γ'/α interface can be derived from recent equilibrium data for the iron-nitrogen phase diagram.[3,24] Thus, the predicted and experimentally determined values for the nitrogen contents agree very well (Table III). The occurrence of equilibrium nitrogen contents at both the surface and the layer/substrate interface indicates that for the advanced stage of layer growth studied here, interface reactions are not rate-determining for the layer growth (*cf.* Reference 25). Instead, diffusion of nitrogen atoms through the layer controls γ' layer growth. This does not need to be true for an early stage of the nitriding process (see References 25 and 26 for further discussion).

For nitrogen diffusion-controlled growth of the γ' layers, a convex or approximately linear nitrogen-concentration depth profile is expected (*cf.* Reference 28), provided that the diffusion coefficient of nitrogen in γ' is practically independent of nitrogen concentration. It is striking to observe that in contrast with this expectation, the nitrogen-concentration depth profile in the surface regions of layers A and B (Figures 6(a) and (b)) is of concave shape. This can be considered as a consequence of the formation of pores in this part of the γ' layers during growth, as will be discussed below.

Porosity in iron-nitrogen phases is very common[6,19,29–31] and can be attributed to the metastability of these phases with respect to molecular nitrogen gas at normal pressures.[19,29] In fact, pores in iron-nitrogen phases can be conceived as "precipitates" of N_2 gas. The driving force for pore formation increases with nitrogen content, causing a first appearance of porosity in the near-surface region of an Fe-N phase produced by inward diffusion of nitrogen into an iron substrate (*cf.* Figures 3(b) and 5(b)). In an early stage of pore formation, isolated pores develop predominantly at grain boundaries. At later stages, coalescence of pores occurs, leading to channels along the grain boundaries in contact with the outer nitriding gas atmosphere. For an isolated pore, it may be expected that adjacent material is impoverished in nitrogen as compared to the pore-free condition. However, in the case of channels, constituents of the outer gas atmosphere can penetrate the channels. Then, the depletion in nitrogen content in an Fe-N phase near a channel (porous grain boundary) can be compensated by uptake of nitrogen atoms due to dissociation of ammonia at the channel walls.* (An extended discussion on nitrogen

*A similar phenomenon of (renewed) uptake of interstitial atoms *via* channels has been observed in ε-$Fe_2(N, C)_{1-x}$ surface layers during nitrocarburizing[6] and explained analogously. In that particular case, the nitrogen depletion was compensated predominantly by uptake of carbon atoms (see Figure 6 and its discussion in Reference 6).

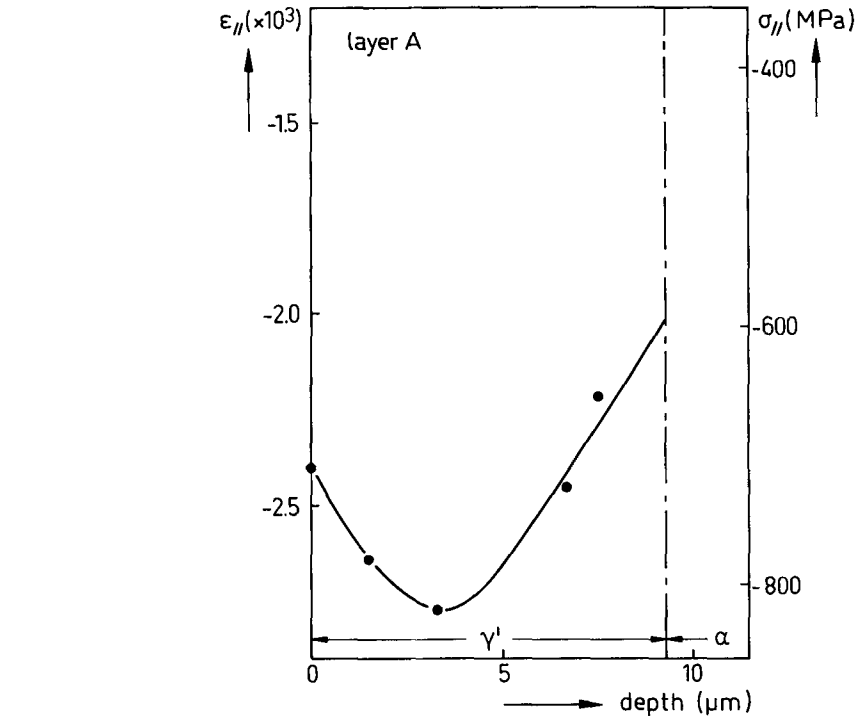

(*a*)

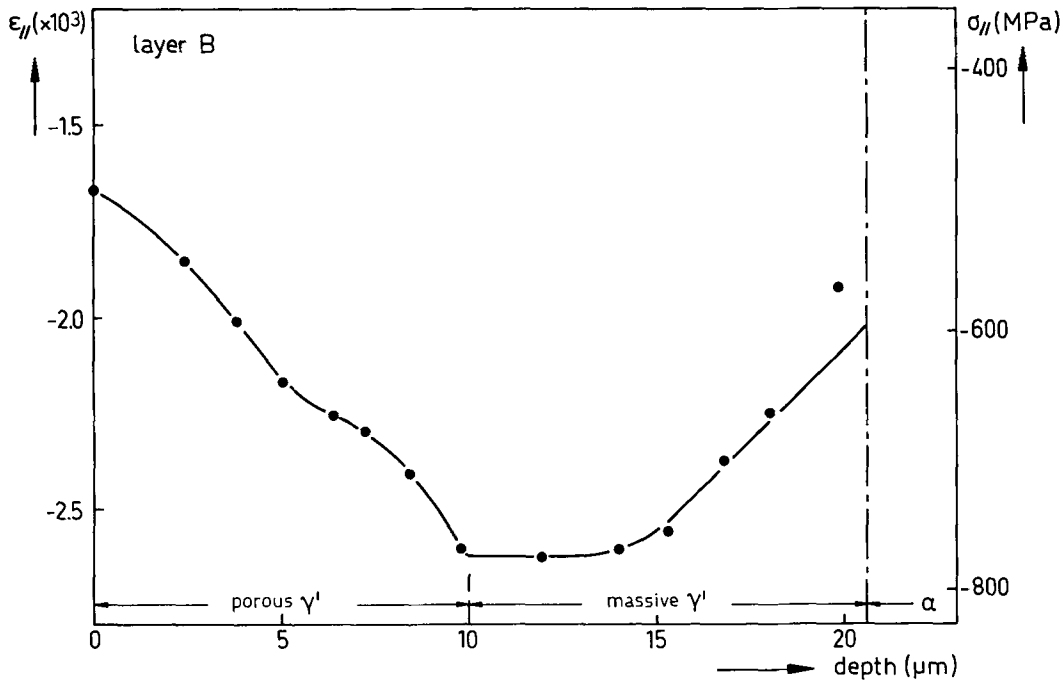

(*b*)

Fig. 5—Dependence of macroscopic strain, $\varepsilon_{//}$, and (macro) stress, $\sigma_{//}$, on depth below the specimen surface, for layers (*a*) A and (*b*) B.

supply *via* channels and its consequences for studies of equilibrium nitrogen absorption in Fe-N phases has been given in Reference 19.)

In the present study, electron-probe microanalysis did not show a significantly smaller nitrogen content in channel/pore-adjacent γ' material, as compared to the bulk value.* It is concluded that the above-discussed uptake of nitrogen atoms through the walls of the channels,

*The N K_α intensity generated was analyzed in an oblique section of layer B along lines parallel to the surface at three depths (*viz.*, 1, 5, and 9 μm) below the surface. A decrease of the N K_α intensity occurring on entering the immediate vicinity of a pore (at distances smaller than 0.5 μm) could be ascribed to a reduction of the amount of material contributing to the N K_α intensity when measuring adjacent to a pore: the incident electron beam had a diameter of about 0.5 μm.

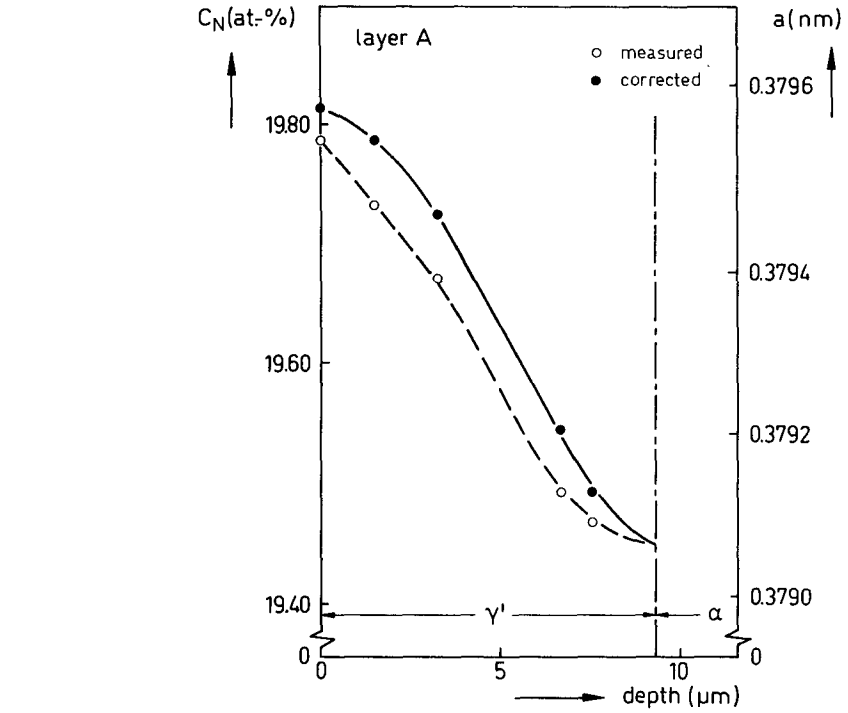

(*a*)

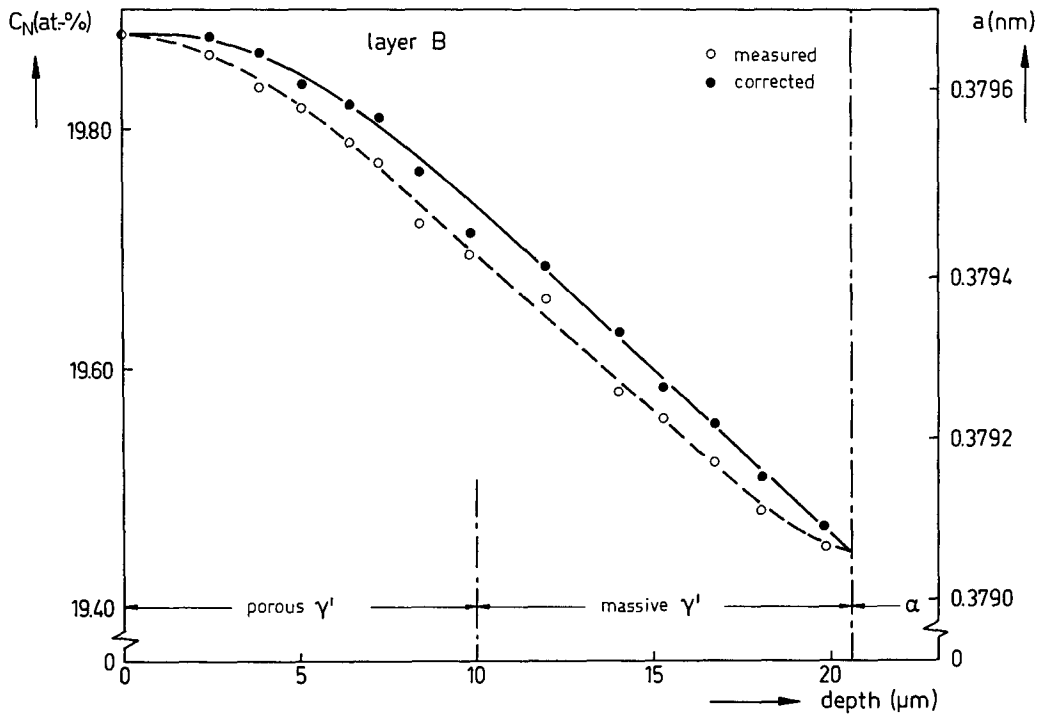

(*b*)

Fig. 6—Dependence of the nitrogen content, c_N, and the strain-free lattice parameter, a, on depth below the specimen surface for layers (*a*) A and (*b*) B. The results before (measured) and after correction (corrected) for the penetration of X-rays have been indicated.

in open contact with the outer gas atmosphere, does occur: the nitriding potential of the outer gas atmosphere is not only imposed on the external surface but also on the internal channel surfaces. As a consequence, concave-shaped nitrogen-concentration depth profiles develop in the porous surface region of a γ' layer.

VI. RESIDUAL STRESSES IN γ'-Fe_4N_{1-x} LAYERS

Clearly, only compressive stresses are observed for both layers (Figures 4 and 5). The dependence of strain on depth is similar for layers A and B. Starting at the layer/

Table III. Predicted and Experimental Nitrogen Contents (Atomic Percent) at the Surface (c_N^s) and at the Interface (c_N^i) of γ' Layers

Layer	c_N^s (Pred.)	c_N^s (Exp.)	c_N^i (Pred.)	c_N^i (Exp.)
A	19.826	19.821	19.454	19.447
B	19.896	19.878	19.454	19.447

substrate interface and proceeding in the direction to the surface, the compressive macroscopic strain increases, passes through a maximum, and eventually decreases in the near-surface part of the layer. In the following, a detailed interpretation of the strain-depth profiles in the γ' layers is presented.

A. *Compositionally Induced Strain Profiles*

The strain, $\varepsilon_{//}$, in the substrate-adjacent regions of the layers A and B is presented as a function of nitrogen composition in Figure 7. Strains within the ragged layer/substrate interface zone (Table II) are not considered in the discussion below for the following reason. After removal of a thin sublayer in the ragged interface region by a mechanical polishing treatment, the microstructure of this section parallel to the surface consists of γ' islands embedded in a ferritic matrix. Since the microhardness of γ'-Fe_4N_{1-x} is much higher than that of ferrite, ferrite is removed to a larger depth than γ' by the mechanical polishing treatment. Hence, the γ' islands protrude from the actual surface, giving rise to (surface) stress relief in γ'. Therefore, stresses determined for the γ' phase within the zone containing the ragged interface are too small, as compared to their original, as-produced value (*cf.* Figure 7).

Apart from the zone containing the ragged interface, the strain data presented in Figure 7 ("open" data points)

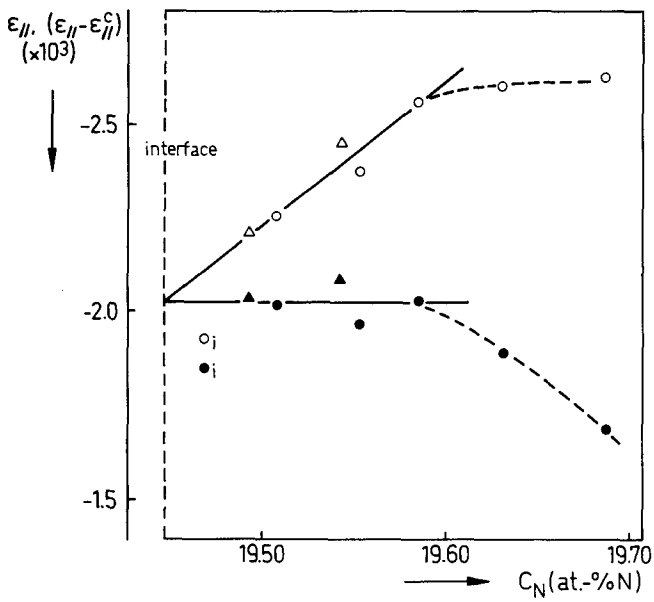

Fig. 7—Dependence of the macroscopic strain, $\varepsilon_{//}$ (open symbols), on composition in the interface-adjacent region of layers A and B. After subtraction of the compositionally induced strain, $\varepsilon_{//}^c$, the strain, $\varepsilon_{//} - \varepsilon_{//}^c$ (filled symbols), remains. Symbols denoted by *i* are within the ragged interface region given by the 95 pct confidence intervals in Table II (see text).

suggest the same (linear) dependence of strain on composition for both layers. Because both layers were produced at the same temperature, the same contribution of thermal misfit to the strain can be expected (Section VI–B). Then, the increase in compressive strain as a function of distance to the γ'/α interface may be ascribed to elastic accommodation of the volume misfit caused by a nitrogen concentration increasing with distance to the interface. This leads to the strain model depicted in Figure 8.

Imagine the γ' layer separated from the substrate and sectioned parallel to the surface into slices of about one unit cell thickness (Figure 8(a)). Provided that the amount of iron atoms is the same in each slice of γ', the unconstrained surface area of a sublayer at some distance from the layer/substrate interface is larger than the unconstrained surface area of a slice directly adjacent to this interface because of the presence of a nitrogen-concentration profile such that the nitrogen concentration increases in the direction to the outer surface of the whole γ' layer. Hence, imposed cohesion between the individual slices such that they adopt, by elastic accommodation, the unconstrained surface area of the slice adjacent to the γ'/α interface (Figure 8(b)) leads to internal stresses. Assuming a state of plane stress for each slice of "infinite" lateral dimensions, a compressive stress parallel to the surface occurs that increases in magnitude with distance to the interface. The corresponding compositional strain, $\varepsilon_{//}^c$, in a slice equals

$$\varepsilon_{//}^c = \frac{a_{int} - a}{a} \cong -\beta_N \cdot \Delta c_N \qquad [5]$$

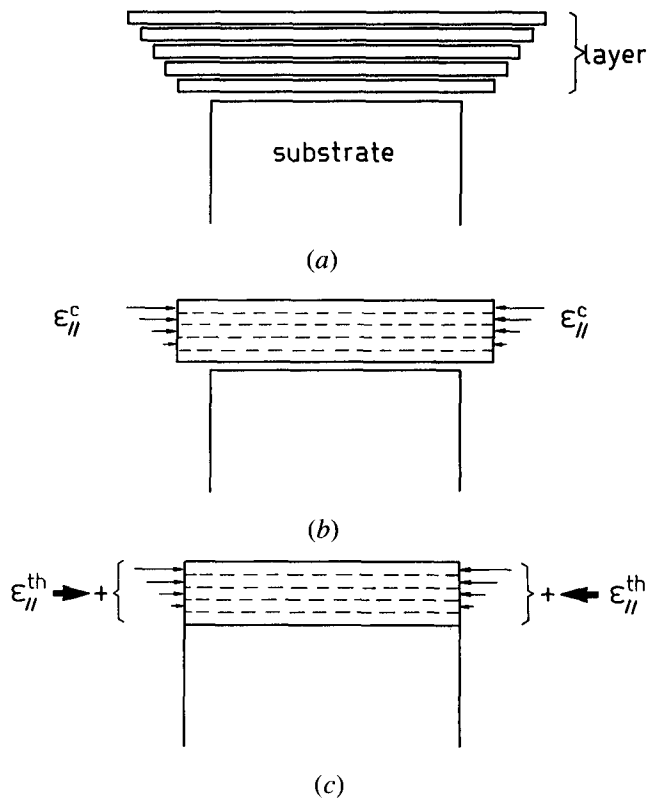

Fig. 8—Schematic representation of compositionally induced, $\varepsilon_{//}^c$ (*b*), and thermally induced, $\varepsilon_{//}^{th}$ (*c*), contributions to the strain-depth profiles in γ' layers.

where a and a_{int} are the strain-free lattice parameters of the slice considered and the interface-adjacent slice, respectively; β_N is the fractional change of the γ'-Fe_4N_{1-x} lattice parameter per unit of nitrogen content (Végard's constant; see Reference 19); and Δc_N denotes the difference in nitrogen content between the γ' slice considered and the interface-adjacent slice.

On this basis, the compositional strain profiles corresponding with the composition profiles presented in Figures 6(a) and (b) can be calculated. Subtraction of the $\varepsilon^c_{//}$ values thus obtained from the "as-determined" (corrected for X-ray penetration; see Section II) $\varepsilon_{//}$ values shows that the same constant compressive strain ($\approx -2.0 \times 10^{-3}$) remains, for both γ' layers, in the interface-adjacent region (Figure 7).

B. *Thermally Induced Strain*

The γ' layer produced by cohesion of the slices in the manner discussed (Figures 8(a) and (b)) and, consequently, containing a compositional stress-depth profile can be fastened on the ferritic substrate. The layer is usually very thin as compared with the substrate. Then, according to a simple model based on elastic behavior, mechanical equilibrium, and a homogeneous distribution of stress due to layer/substrate misfit, it follows that the layer will assimilate virtually all layer/substrate misfit strain (Appendix C). This uniform strain contribution due to layer/substrate misfit is superimposed on the compositional strain-depth profile in the layer (Figure 8(c)).

Two possible origins for layer/substrate misfit leading to a compressive strain contribution in the layer can be considered:

(1) a *volume misfit* because of different specific volumes per solvent (= iron) atom of α and γ' phases and
(2) a *thermal misfit* because of different thermal contractions of layer and substrate on cooling from the nitriding temperature (843 K) down to room temperature (293 K).

Elastic accommodation of the interfacial volume misfit between γ' and α at the nitriding temperature would lead to a strain in γ' (parallel to the interface) given by $\varepsilon^{vol}_{//} = -46 \times 10^{-3}$ (as derived from lattice-parameter data provided in References 19 and 32), which is, in an absolute sense, 23 times as high as the experimental value ($\varepsilon_{//} - \varepsilon^c_{//} \approx -2.0 \times 10^{-3}$; see above and Figure 7). Plastic accommodation of volume misfit between layer and substrate could be achieved by appropriate adaptation of the thickness of the layer during growth. This has been suggested for dual-phase ε/γ' compound layers on ferrite.[5] This also pertains to the present case of γ' layer growth on ferrite, as follows from experimental evidence obtained in this work: from the measured nitriding-produced increase of the thickness of the whole specimen and the measured thickness of the γ' layer separately, it has been calculated that the γ' layer obtained is 17 pct thicker (for specimen B) than the original α-iron layer of the substrate converted into γ' on nitriding. Since the volume of γ' per iron atom is 16 pct larger than the volume of α per iron atom, it can be concluded that $\varepsilon^{vol}_{//}$ is indeed accommodated completely by adaptation of the γ' layer thickness on nitriding.

The thermal misfit at a layer/substrate interface originates from linear expansion coefficients different for layer and substrate. The associated thermal strain in γ' parallel to the surface, $\varepsilon^{th}_{//}$, induced on cooling from the nitriding temperature, T_1, down to room temperature, T_2, can be calculated from

$$\varepsilon^{th}_{//} = \int_{T_1}^{T_2} (\alpha_{\gamma'} - \alpha_{Fe}) \cdot dT \qquad [6]$$

where $\alpha_{\gamma'}$ and α_{Fe} are the linear thermal expansion coefficients for layer and substrate, respectively. Using literature data for $\alpha_{\gamma'}$ and α_{Fe},[19,33] it follows for the strain $\varepsilon^{th}_{//} = -3.9 \times 10^{-3}$, which is of the same order of magnitude as the strain value obtained by subtracting $\varepsilon^c_{//}$ from $\varepsilon_{//}$ at the interface (see above; $\varepsilon_{//} - \varepsilon^c_{//} \approx -2.0 \times 10^{-3}$). If the experimental strain, $\varepsilon_{//} - \varepsilon^c_{//}$, is fully ascribed to thermal misfit between layer and substrate, then, according to Eq. [6], the temperature from which strain buildup would have taken place on cooling equals 620 K, whereas the nitriding temperature equals 843 K. This discrepancy can be discussed as follows.

During the cooling (not quenching; see Section III–A) from the nitriding temperature, α-Fe precipitates develop in the γ' nitride layer and γ'-Fe_4N_{1-x} and α''-$Fe_{16}N_2$ precipitates develop in the ferrite substrate (*cf.* phase diagram[3,24]). In general, phase transformations can lead to relaxation or development of internal stresses (see, *e.g.*, Reference 34). For internally stressed γ'-Fe_4N_{1-x} layer/α-Fe substrate assemblies, quenched after nitriding, it has been shown that on nonisothermal heating, strain relaxation occurs at about 600 K, which is rate-controlled by the precipitation of α-Fe in the substrate-adjacent part of the γ' layer.[35] Hence, for the present specimens, it is suggested that the latter process is responsible for the accommodation of the thermal misfit built up on cooling from the nitriding temperature down to about 600 K.

C. *Stress Relaxation in the Surface-Adjacent Region of the Layer Due to Pores/Channels*

The decrease of the value of the compressive macroscopic strain near the surface, as observed on proceeding from layer/substrate interface to layer surface, coincides with the occurrence of pores/channels in both layers (see Section IV, the t_p values in Table II, and Figures 5(a) and (b)). As discussed in Section V, pore/channel formation occurs in particular in the near-surface region at grain boundaries. The latter are usually perpendicular to the surface (*cf.* Figures 3(a) and (b)), which is a normal mode of diffusional layer growth.

Because of mechanical equilibrium with respect to the laboratory frame of reference, the stress component perpendicular to the internal channel surfaces equals zero. Consequently, the imposition of compositionally and thermally induced strains, as discussed for the massive part of the layers in Sections VI–A and B, leads to strain gradients parallel to the surface in the surface-adjacent region of the layers where channels occur. This is shown schematically in Figure 9 by means of isostress contours. Here, the outer part of the layer is conceived as an assembly of "free-standing columns."[36,37] As a result, the average compressive strain/stress parallel to the surface in the near-surface region will be smaller than

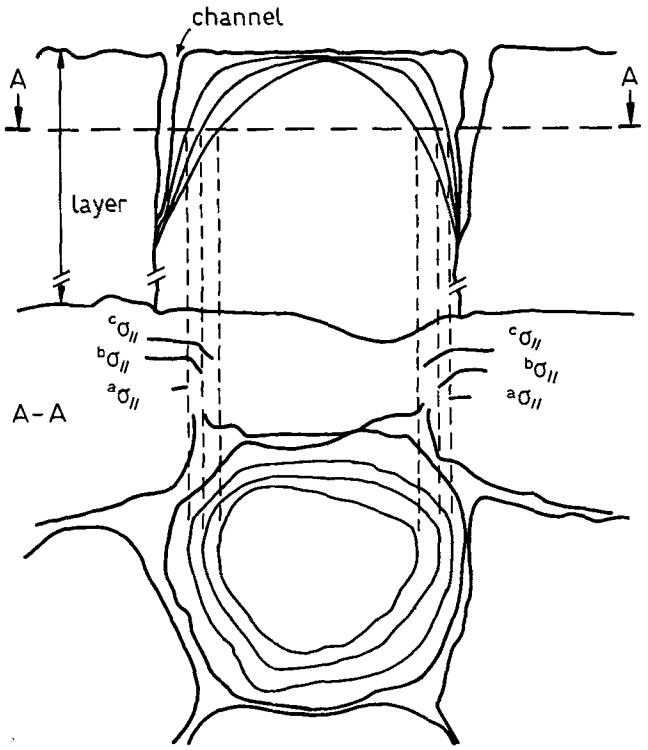

Fig. 9—Schematic isostress contours in porous part of a γ' layer as viewed in a cross section (upper part of figure) and as viewed from the top in the section parallel to the surface denoted by A-A (lower part of figure): $|^{a}\sigma_{//}| < |^{b}\sigma_{//}| < |^{c}\sigma_{//}|$.

for a corresponding massive layer. This effect is denoted as relaxation in the present paper. In the following, it will be shown that a consistent interpretation of the X-ray diffraction data is possible on this basis.

1. *Integral breadth*

The integral breadth, β, *i.e.*, the integrated intensity (peak area) divided by the intensity at the peak of the line profile, can be used as a measure for line broadening. Experimental data for β of the $\{420\}_{\gamma'}$ line profile for $\psi = 0$ are depicted in Figure 10(a) as a function of depth below the surface in layer B. Clearly, the value for the integral breadth is significantly larger for the porous near-surface region than for the massive part.

Neither composition variations parallel (electron-microprobe data; Section V) and perpendicular (Figure 6(b); information depth for $\psi_0 = 1.3$ μm) to the surface nor strain-depth gradients (Figure 5(b); note similar gradient in massive, bottom region) can explain the additional line broadening for the surface region. Hence, this extra line broadening is due to lattice-spacing variations parallel to the surface, indicating strain relaxation due to the presence of channels.

2. *Asymmetry of line broadening*

If the simultaneously diffracting volumes of "relaxed" and "constrained" material (*cf.* Figure 9) in the part of the layer probed are unequal, asymmetric line broadening can be expected. As long as the amount of relaxed material is relatively small, broadening occurs to the side of the position of the Bragg angle for strain-free material.

Asymmetry is observed for γ' {420} line profiles recorded at the original surface for $\psi = 0$ (Figure 10(b)).

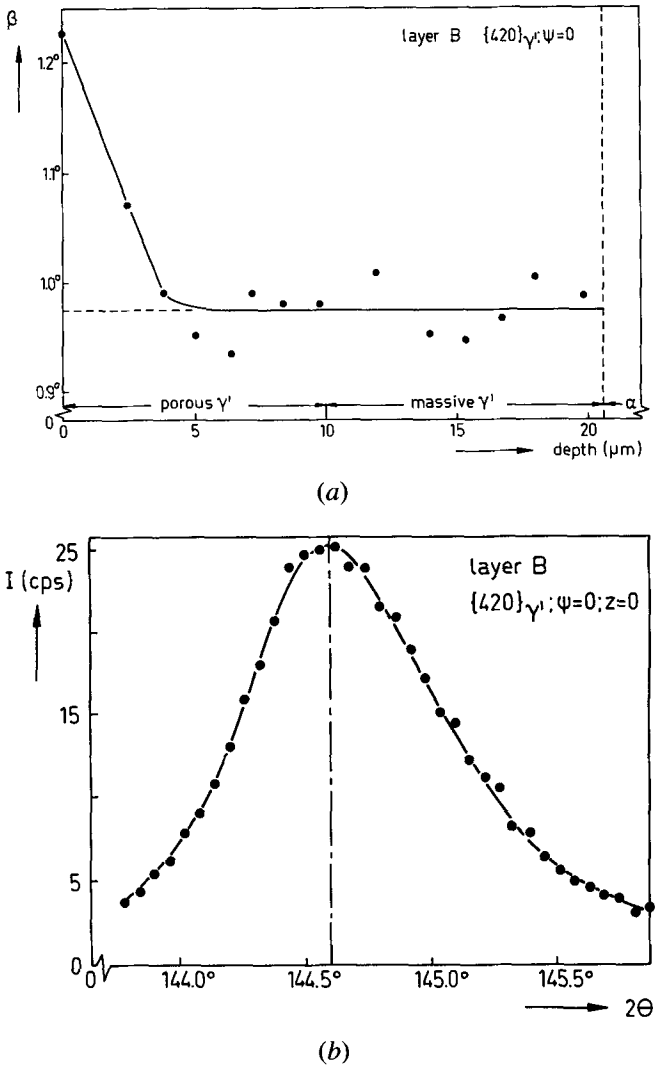

Fig. 10—(*a*) Integral breadth, β, of $\{420\}_{\gamma'}$ line profile for layer B as a function of the total removed sublayer thickness. No correction was made for penetration of the X-rays. (*b*) Part of $\{420\}_{\gamma'}$ line profile recorded at the original surface of layer B for $\psi = 0$. Asymmetrical broadening occurs at the high-angle side, where the Bragg angle (2θ), corresponding with the strain-free lattice parameter, resides (at $2\theta = 145.3$ deg).

Because the average stress parallel to the surface is of a compressive nature and since at $\psi = 0$ the spacing is measured in the direction perpendicular to the surface, the Bragg angle for strain-free material occurs at the high-angle side of the peak. Indeed, broadening at the high-angle side of the profile is stronger than at the low-angle side (the occurring broadening is very much larger than that due to instrumental effects; see Figure 10(a)).*

*Asymmetry may also be caused by the strain (stress)-depth gradients (compositional variations are practically absent in the material analyzed; see above). However, it follows from the (d_ψ, z) curves that for $\sin^2 \psi = 0$, d_ψ increases with depth up to $z = 6.4$ μm (Figure 4(b)). Then, in view of the absorption of X-rays, line broadenings at $\psi = 0$ would occur with an asymmetry opposite to the observed one.

3. *Curvature in (d_ψ, $\sin^2 \psi$) plots*

Removal of a sublayer leads to a redistribution of stress. Then, after correction for penetration of X-rays by method (2) in Section II, in principle, curvature remains in the

(d_ψ, $\sin^2 \psi$) plots. For a massive sublayer, this curvature can be ignored (Appendix C). However, this need not hold for removal of a sublayer from the outer, porous part of the γ' layers. This can explain the curvature in the (d_ψ, $\sin^2 \psi$) plot of layer B for zero depth in Figure 4(b) (case of most porosity).

4. *Depth dependence of relaxation*

For a thin layer composed of "free-standing columns," the amount of relaxed material decreases with increasing distance away from the surface of the layer (*cf.* Figure 9).[36,37] This explains largely that the observed extent of relaxation for the γ' layers decreases for increasing distance away from the surface (Figures 5(a) and (b)). However, it is remarkable that for layer B the additional line broadening (Section VI–C–1) and the curvature in the (d_ψ, $\sin^2 \psi$) plots (Section VI–C–3) vanish for depths larger than about 5 μm, while relaxation and porosity are observed until a depth of about 10 μm (Figure 5(b); Table II). This can be attributed to incomplete coalescence of the pores at the grain boundaries in the bottom part of the porous zone. In addition, it is noted that a kink occurs at a depth of about 5 μm in the curve of strain *vs* depth for layer B (Figure 5(b)). This kink can be a consequence of the stress redistribution in each free-standing column upon sublayer removal: for the present case, ignoring the minor curvature in the corresponding (d_ψ, $\sin^2 \psi$) plot implies that the absolute value for $\varepsilon_{//}$ is somewhat underestimated.

5. *Biaxial or triaxial description of the state of stress*

Actually, the overall state of stress in the surface-adjacent region of layer B is not purely biaxial because of the relaxation effects. Due to anticipated rotational symmetry of the overall state of stress and, in any case, because of specimen rotation applied during the diffraction experiments (Section III–B), the stress components σ_{ij} with $i \neq j$ are *nil*, leaving σ_{33} as the only additional stress component to be considered.

The nitrogen composition at the surface of the γ' layer has been obtained in Section V by interpolation in the (d_ψ, $\sin^2 \psi$) plot for the strain-free direction indicated by $\sin^2 \psi_0 = 0.497$ for an assumed biaxial state of stress ($\sigma_{//} \equiv \sigma_{11} = \sigma_{22}$). The difference with the predicted value for layer B, where porosity is most severe, is only 1.8×10^{-2} at. pct N (Table III). The experimental inaccuracy is estimated as 1.6×10^{-2} at. pct (*cf.* Section IV). This already suggests the relative unimportance of σ_{33}. For quantification, it will be assumed that the nitrogen content at the surface, as predicted from the literature data, is the true value (Table III). Then, by interpolation in the corresponding (d_ψ, $\sin^2 \psi$) plot, an experimental value for the strain-free direction is obtained: $\sin^2 \psi_0 = 0.462$. For a triaxial state of stress with $\sigma_{//} \equiv \sigma_{11} = \sigma_{22}$, σ_{33}, and $\sigma_{ij} = 0$ for $i \neq j$, it follows for the strain-free direction (*cf.* Reference 38) that

$$\sin^2 \psi_0 = -\frac{2\sigma_{//} + \sigma_{33}}{\sigma_{//} - \sigma_{33}} \cdot \frac{S_1}{\frac{1}{2} S_2} - \frac{\sigma_{33}}{\sigma_{//} - \sigma_{33}} \qquad [7]$$

Using the experimental value for $\sin^2 \psi_0$ given above, it is obtained for the state of stress at the outer surface of layer B, where most porosity occurs: $\sigma_{33} \approx 1/8 \cdot \sigma_{//}$. Hence, the state of stress in the layer is effectively biaxial.

VII. CONCLUSIONS

1. *Determination of stress- and composition-depth profiles.* Stress- and composition-depth profiles in γ'-Fe_4N_{1-x} surface layers on α-Fe substrates have been determined by X-ray diffraction analysis. A change in nitrogen content of only about 0.45 at. pct on a total of about 20 at. pct could be established in about 15 steps over a total layer thickness of about 20 μm. The associated maximum change in stress is about 300 MPa, including a reversal of sign of the stress gradient. At present, no other technique allows a comparable depth resolution.
2. *Composition-depth profiles.* Equilibrium values for the nitrogen contents occur at the outer surface of the layer and at the layer/substrate interface, indicating diffusion-controlled growth of the γ' compound layer. During nitriding, metastability of γ' causes "precipitation" of N_2 gas as pores at grain boundaries, in particular in the surface-adjacent region. On prolonged nitriding, coalescence of such pores leads to channels (open grain boundaries). Smoothing away of the nitrogen-concentration gradient in the near-surface, porous region of γ'-Fe_4N_{1-x} surface layers is caused by lateral inward diffusion of nitrogen through walls of the channels at grain boundaries in open contact with the nitriding gas atmosphere.
3. *Development of residual stresses.* In the massive bottom part of the γ' layer, a compressive stress parallel to the surface occurs, which increases in magnitude with increasing distance to the layer/substrate interface. This stress profile is caused by elastic accommodation of the change in nitrogen content within the layer. In addition, accommodation of the cooling-induced misfit between layer and substrate, arising from different thermal contractions of layer and substrate on cooling from the production temperature to the measurement temperature, contributes to the residual stresses in the layer. The change in specific volume per iron atom on conversion of α-iron into γ' nitride is accommodated by adaptation of the γ' layer thickness during nitriding.
4. *Relaxation of residual stresses.* In the surface-adjacent part of the γ' layer, the compressive stress parallel to the surface decreases with decreasing distance to the surface. Due to the presence of channels in this region, the imposition of compositionally and thermally induced strains leads to average stresses parallel to the surface smaller than those of corresponding massive material. The X-ray diffraction observations indicate the presence of strain gradients parallel to the surface associated with stress relaxation.

APPENDIX A

Ghost-stress effects in γ'-Fe_4N_{1-x} compound layers on α-Fe

A hypothetical 10-μm-thick γ'-Fe_4N_{1-x} surface layer is considered here. The strain-free lattice parameter, a,

is taken as a linear function of the depth, z_s, below the original surface:

$$a = 0.37960 - 5.438 \times 10^{-3} \times z_s$$

(a in nm; z_S in μm)

Ill-considered fitting of straight lines to $(d_\psi, \sin^2 \psi)$ data (*cf.* Eq. [1]), as could be obtained from such surface layers, leads to erroneous values for the stress, because the effective depth below the surface probed by the X-rays depends on ψ. The treatment is performed for cases of presence and absence of a stress-depth profile (state of plane stress). In the absence of a stress profile, the relation between "true" lattice spacing, d_ψ, and depth below the occurring surface, z, does not depend on ψ (case a), in contrast with the presence of a stress profile (case b).

a. *Stress-free γ'-Fe_4N_{1-x} layer containing a linear lattice spacing-depth profile*

The "measured" lattice spacing, $\langle d \rangle$, for different values of ψ ($0 \leq \sin^2 \psi \leq 0.6$) after removal of a thin γ' sublayer can be calculated from Eq. [3], taking t as the *remaining* surface layer thickness (see also Eq. [B1]). The geometric factor, k, in Eq. [3] was taken as that valid for an ω goniometer, *i.e.*,[9,10]

$$k = 2 \frac{\sin \theta \cos \omega}{\sin^2 \theta - \sin^2 \omega} \qquad [A1]$$

Ghost stresses were calculated from the slopes of the straight lines fitted (least-squares analysis) through the $(\langle d \rangle_\psi, \sin^2 \psi)$ data.

The above calculations were carried out for various characteristic X-ray wavelengths; the data used are gathered in Table AI. In all cases, the $\{hkl\}_{\gamma'}$ reflection was chosen at the highest possible Bragg angle ($\theta \leq 80$ deg). Corresponding X-ray elastic constants were the same as those given in Section IV.

The ghost stress calculated, $\langle \sigma \rangle$, is shown as a function of depth below the original surface (= total removed sublayer thickness, Δt) in Figure A1. Obviously, small ghost stresses are expected if a minor penetration of X-rays occurs (*i.e.*, strong absorption): see results for Co K_β and Cu K_{α_1} in Figure A1.

The values for the ghost stresses as calculated for Co K_{α_1} are strikingly small in view of the relatively small linear absorption coefficient of γ'-Fe_4N for this wavelength (Table AI). This can be understood as follows. For this particular combination of μ and t values, the effective depth probed by the X-rays does not depend strongly on tilt angle ψ, as is illustrated by values calculated for the information depth (Eqs. [8] and [9] in

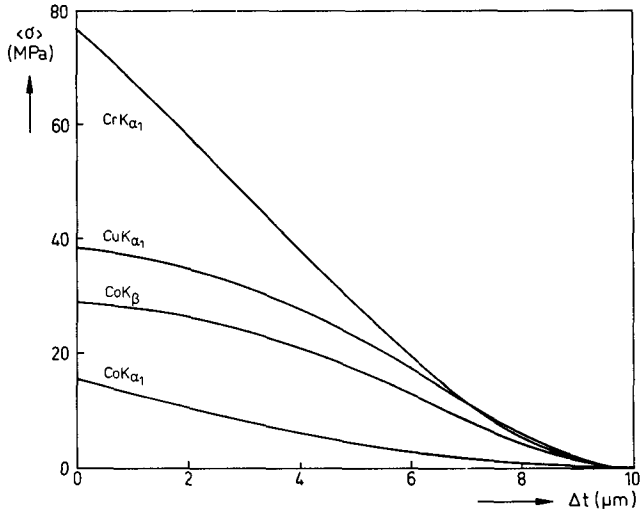

Fig. A1—Ghost stress, $\langle \sigma \rangle$, as a function of the total sublayer thickness removed, Δt; calculated for a hypothetical strain-free γ' layer with a linear composition-depth profile for various characteristic X-ray wavelengths.

References 9 and 16, respectively). Then, because the lattice spacing, d, does not depend on ψ here, only a minor ghost stress arises. For the stress-free γ'-Fe_4N_{1-x} layers much thicker than 10 μm, appreciable ghost stresses do occur for Co K_{α_1} too (compare the shape of curves for Cr K_{α_1}, Cu K_{α_1}, and Co K_β with that for Co K_{α_1} in Figure A1).

b. *γ'-Fe_4N_{1-x} layer containing composition- and stress-depth profiles*

The stress profile, as induced by the fully elastic accommodation of the hypothetical linear concentration profile, leads to a lattice-spacing variation, different for each ψ, superimposed on that inherent to the concentration profile. For calculation of this stress profile, denoted by $\sigma^c_{//}(z_s)$, see Section V; in particular, Eqs. [4] and [5]. Substitution of $\sigma^c_{//}$ values in Eq. [1] gives lattice-spacing values, d_ψ. The "measured" lattice spacings were subsequently calculated by using Eq. [3] after each imaginary sublayer removal (analogous to the procedure employed in subsection a). Then, stress values were calculated from the slopes of the straight lines fitted (least-squares analysis) through the $(\langle d \rangle_\psi, \sin^2 \psi)$ data.

The ghost stress obtained, $(\langle \sigma \rangle - \sigma^c_{//})$, is given as a function of depth below the original surface (= total removed sublayer thickness, Δt) in Figure A2 for different characteristic X-ray wavelengths (*cf.* Table AI). Clearly, Co K_β and Cu K_{α_1} radiation are preferred for

Table AI. Data Concerning Different X-Ray Wavelengths Used for Calculation of Ghost Stresses

Radiation	λ (nm)	μ (μm^{-1})	$\{hkl\}$	S_1 (10^{-6} MPa^{-7})	(1/2) S_2 (10^{-6} MPa^{-7})	$\sin^2 \psi_0$
Cu K_{α_1}	0.1540562	0.2070	420	−1.75	7.04	0.497
Cr K_{α_1}	0.2289700	0.0778	220	−1.41	6.03	0.469
Co K_{α_1}	0.1788965	0.0387	400	−2.35	8.83	0.532
Co K_β	0.1620790	0.2349	420	−1.75	7.04	0.497

Note: λ = wavelength; μ = linear absorption coefficient; $\{hkl\}$ = Miller indices of γ' reflection chosen; S_1 and (1/2) S_2 are the X-ray elastic constants; ψ_0 = strain-free direction (data from Ref. 20; see also Section IV).

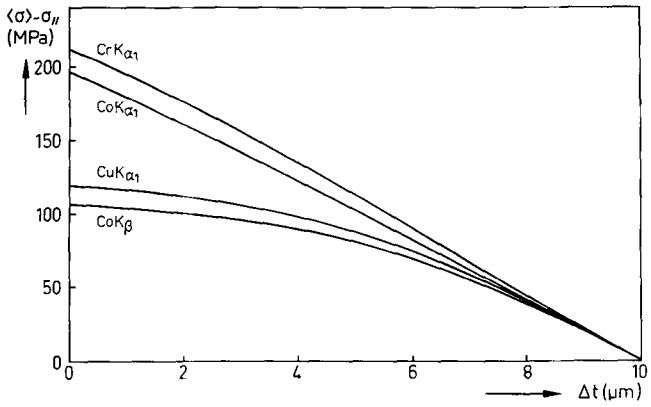

Fig. A2—Ghost stress, $\langle\sigma\rangle - \sigma^c_{//}$, as a function of the total sublayer thickness removed, Δt; calculated for a hypothetical γ' layer containing a linear composition-depth profile and the corresponding compositionally induced stress-depth profile, for various characteristic X-ray wavelengths.

minimization of ghost-stress effects on measurement. Nevertheless, the magnitude of the ghost stresses obtained at $z_s = 0$ ($\Delta t = 0$) for these radiations does amount to 25 to 30 pct of the total change of stress over the thickness of the hypothetical layer, illustrating the necessity of a correction for the effect of X-ray penetration (see Section II and Appendix B).

With reference to the discussion on the relatively small ghost stresses calculated for Co K_{α_1} in case a, the occurrence of the relatively large ghost stresses in case b can be understood, because now the relatively large information depth for Co K_{α_1} is combined with the presence of a strain-depth profile.

APPENDIX B

Correction for the penetration of X-rays in surface layers

Consider a surface layer of total thickness t. After removal of n sublayers with an accumulated thickness t_n ($<t$), the lattice spacing observed from the actual surface, $\langle d\rangle_n$, conforms to (*cf.* Eq. [3])

$$\langle d\rangle_n \int_0^{t-t_n} \exp\{-\mu k z\}\cdot dz = \int_0^{t-t_n} d(z)\cdot\exp\{-\mu k z\}\cdot dz \qquad [B1]$$

where z denotes the depth beneath the instantaneous surface at t_n. Similarly, after removal of the next sublayer ($t_n < t_{n+1} < t$),*

$$\langle d\rangle_{n+1} \int_0^{t-t_{n+1}} \exp\{-\mu k z'\}\cdot dz' = \int_0^{t-t_{n+1}} d(z')\cdot\exp\{-\mu k z'\}\cdot dz' \qquad [B2]$$

*It is assumed that for ψ = constant (*cf.* Section II), k does not change significantly within $[t_n, t_{n+1}]$.

where z' denotes the depth beneath the instantaneous surface at t_{n+1}. Subtraction of Eq. [B2] from Eq. [B1] gives (note: $z' = z + (t_n - t_{n+1})$)

$$\langle d\rangle_n \int_0^{t_{n+1}-t_n} \exp\{-\mu k z\}\cdot dz + [\langle d\rangle_n - \langle d\rangle_{n+1}] \times \int_{t_{n+1}-t_n}^{t-t_n} \exp\{-\mu k z\}\cdot dz = \int_0^{t_{n+1}-t_n} d(z)\cdot\exp\{-\mu k z\}\cdot dz \qquad [B3]$$

Now, consider $t_{n+1} - t_n$ as an infinitesimal distance: $(t_{n+1} - t_n) \to dz$. Then,

$$\langle d\rangle_n \cdot 1\cdot dz + [\langle d\rangle_n - \langle d\rangle_{n+1}]\cdot\left\{\frac{1-\exp\{-\mu k(t-t_n)\}}{\mu k}\right\} = d_n\cdot 1\cdot dz \qquad [B4]$$

and also

$$\langle d\rangle_n - \langle d\rangle_{n+1} = -\left.\frac{\partial\langle d\rangle}{\partial z}\right|_{t_n}\cdot dz \qquad [B5]$$

Finally, it is obtained:

$$d_n = \langle d\rangle_n - \left.\frac{\partial\langle d\rangle}{\partial z}\right|_{t_n}\cdot\left\{\frac{1-\exp\{-\mu k(t-t_n)\}}{\mu k}\right\} \qquad [B6]$$

Note that the term between braces equals the "equivalent thickness" (see Eq. [7] in Reference 9).

APPENDIX C

Effect of sublayer removal on the strain determined in surface layers

Consider a specimen of infinitely large lateral dimensions that is composed of a relatively thick substrate of thickness $2h$ and relatively thin surface layers each of thickness t on either surface of the substrate (Figure C1). At the layer/substrate interface, a misfit, ε, exists, which

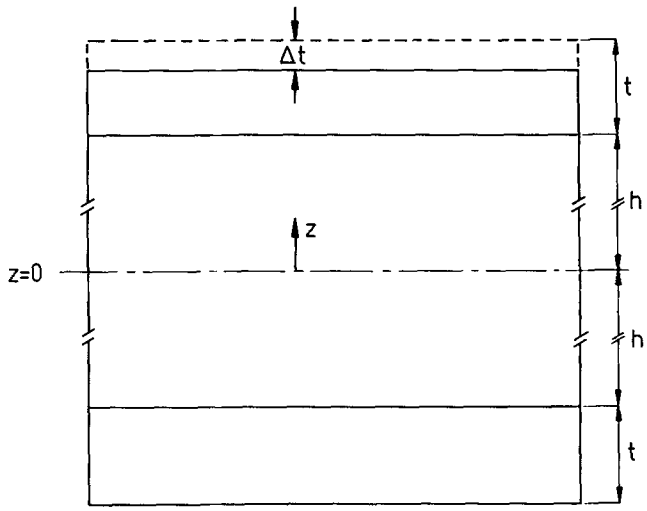

Fig. C1—Layer/substrate/layer geometry; $z = 0$ denotes the midplane; Δt = sublayer thickness removed.

is, for example, generated by different thermal contractions of layers and substrate on cooling from layer-production temperature to room temperature. For the purpose of illustration, the initial strains in both layers, as well as the substrate, are taken constant. Then, for full elastic accommodation of the misfit, mechanical equilibrium requires that the strains in layers and substrate, $\varepsilon^l_{//}$ and $\varepsilon^s_{//}$ ($\varepsilon^l_{//} = \varepsilon^s_{//} + \varepsilon$), are given by (state of plane stress; balance of forces)

$$\varepsilon^l_{//} = \frac{E'_s h}{E'_l t + E'_s h}\,\varepsilon \qquad [C1]$$

$$\varepsilon^s_{//} = \frac{-E'_l t}{E'_l t + E'_s h}\,\varepsilon \qquad [C2]$$

where $E' = E/(1 - \nu)$ with E and ν as Young's modulus and Poisson's constant, respectively.

Now, remove a sublayer of thickness Δt ($<t$) from one of the surface layers. As a consequence of the disturbance of the initial balance of moments, a constant curvature of the specimen will be evoked on settlement of the new mechanical equilibrium. If $2h + (2t - \Delta t) \gg \Delta t$, the state of stress can still be taken as planar (minor curvature). The change in strains for layers and substrate can then be calculated as follows. A bending-induced depth gradient for the strains $\varepsilon^s_{//}$ and $\varepsilon^l_{//}$ is introduced, which is constant over the specimen thickness. Consequently,

$$\varepsilon^l_{//}(z) = az + b + \varepsilon \qquad [C3a]$$

$$\varepsilon^s_{//}(z) = az + b \qquad [C3b]$$

where z is the distance to the original midplane parallel to the surface of the specimen. Requiring balancing of the forces and the moments along z within the specimen, a and b can be calculated. It is obtained with $a = p \cdot \varepsilon$ and $b = q \cdot \varepsilon$:

$$p = \frac{C_2K_3 + C_3K_1}{C_1K_1 - C_2K_2} \qquad [C4a]$$

$$q = \frac{C_3K_2 + C_1K_3}{C_1K_1 - C_2K_2} \qquad [C4b]$$

with

$$C_1 = \frac{1}{3}E'_l[t\{3h^2 + 3th + t^2\} + (t - \Delta t) \cdot \{3h^2 + 3(t - \Delta t)h + (t - \Delta t)^2\}] + \frac{2}{3}E'_s h^3$$

$$C_2 = C_3 = K_2 = \frac{1}{2}E'_l[2h + 2t - \Delta t]$$

$$K_1 = E'_l(2t - \Delta t) + 2E'_s h$$

$$K_3 = -E'_l(2t - \Delta t)$$

Similarly, equations can be derived for the case when more material than corresponding with one entire surface layer has been removed ($\Delta t > t$).

As an example, the following case is analyzed. The misfit strain between layer and substrate amounts to $\varepsilon = -2 \times 10^{-3}$; the thickness of the substrate is taken as 2 mm, and layer thicknesses of 10 and 20 μm are used. Further, E'_l and E'_s amount to 0.295×10^6 MPa (Section IV) and 0.299×10^6 MPa,[23] respectively. (Thus, the thermal misfit in the present γ'-Fe_4N_{1-x} layers can be modeled (Section VI–B).) The strain at the occurring surface is given as a function of the removed sublayer thickness, Δt, in Figure C2. It is concluded that (1) practically all misfit strain is accommodated by the layer and (2) for $\Delta t > 0$ the maximum change in $\varepsilon^l_{//}$ by sublayer removal is only a few percent of the value for $\Delta t = 0$ (*e.g.*, for $\Delta t = 20$ μm for a layer of 20-μm thickness originally: 4 pct change).

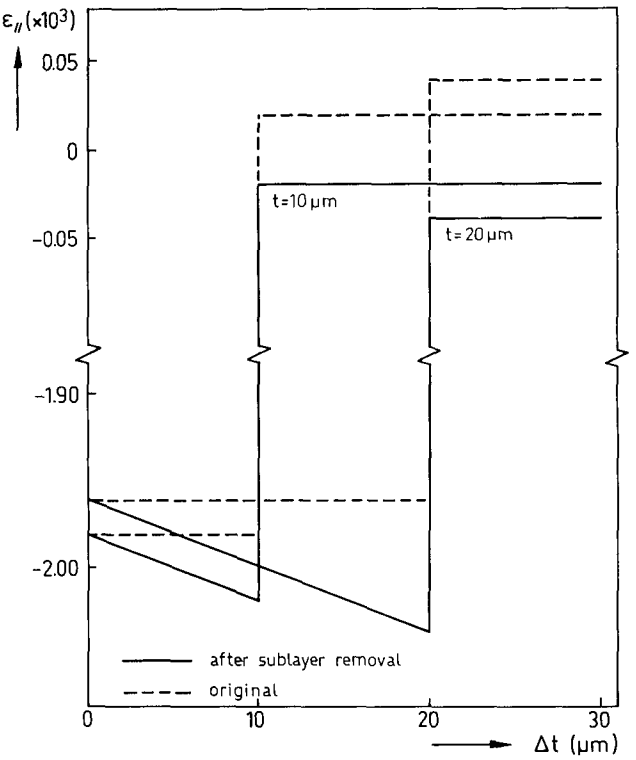

Fig. C2—Strain at the occurring surface, $\varepsilon_{//}$, as a function of the removed sublayer thickness, Δt, for cases of γ' layers of 10- and 20-μm thickness on both faces of a ferrite substrate of 2-mm thickness. Dotted lines represent original strain-depth profiles in as-produced layer/substrate/layer assemblies.

The curvature in (d_ψ, $\sin^2 \psi$) plots for the surface region of layer B, after correction for X-ray penetration according to method (2), could be caused by this effect of stress redistribution upon sublayer removal. However, the change of lattice spacing, d_ψ, due to removal of a massive sublayer, as discussed above, is an order of magnitude smaller than the deviation of individual d_ψ data from the straight line fitted to the (d_ψ, $\sin^2 \psi$) data (*cf.* Sections IV and VI–C).

ACKNOWLEDGMENTS

We are indebted to Ir. W.G. Sloof and Professor B.M. Korevaar for discussions. We are obliged to Dr. Ir. Th.H. de Keijser and Ing. N.M. van der Pers for discussions, provision of X-ray facilities, and technical assistance. Ir. D. Schalkoord performed electron-probe microanalysis. Ir. L.E. Gooijer of Eindhoven University of

Technology is thanked for discussion on strain relaxation by sublayer removal. Financial support of the Foundation for Fundamental Research of Matter (FOM) is gratefully acknowledged.

REFERENCES

1. *Residual Stress for Designers and Metallurgists*, L.J. Vande Walle, ed., ASM, Metals Park, OH, 1981.
2. *Source Book on Nitriding*, ASM, Metals Park, OH, 1977.
3. O. Kubachewski: *Iron-Binary Phase Diagrams*, Springer-Verlag, Berlin, 1982, pp. 67-70.
4. H.C.F. Rozendaal, P.F. Colijn, and E.J. Mittemeijer: *Surf. Eng.*, 1985, vol. 1, pp. 30-42.
5. H. Oettel and B. Ehrentraut: *Härterei-Tech. Mitt.*, 1985, vol. 40, pp. 183-87.
6. M.A.J. Somers and E.J. Mittemeijer: *Surf. Eng.*, 1987, vol. 3, pp. 123-37.
7. H. Dölle and V. Hauk: *Härterei-Tech. Mitt.*, 1976, vol. 31, pp. 165-68.
8. H. Dölle: *J. Appl. Crystallogr.*, 1979, vol. 12, pp. 489-501.
9. R. Delhez, Th.H. de Keijser, and E.J. Mittemeijer: *Surf. Eng.*, 1987, vol. 3, pp. 331-42.
10. V. Hauk and E. Macherauch: in *Residual Stresses in Science and Technology*, V. Hauk and E. Macherauch, eds., DGM Informationsgesellschaft mbH, Oberursel, Federal Republic of Germany, 1987, pp. 243-55.
11. *Residual Stress Measurement by X-ray Diffraction*, Report No. SAE J784a, 2nd ed., SAE, Warrendale, PA, 1971.
12. H. Dölle and V. Hauk: *Härterei-Tech. Mitt.*, 1979, vol. 34, pp. 272-77.
13. R.A. Prümmer and H.W. Pfeiffer-Volmar: *Adv. X-Ray Anal.*, 1983, vol. 26, pp. 225-31.
14. T.S. Lei and J.T. Scardina: in *Microstructural Science*, Elsevier, New York, NY, 1976, pp. 269-80.
15. C.N.J. Wagner, M.S. Boldrick, and V. Perez-Mendez: *Adv. X-Ray Anal.*, 1983, vol. 26, pp. 275-82.
16. W.G. Sloof, M.A.J. Somers, R. Delhez, Th.H. de Keijser, and E.J. Mittemeijer: in *Residual Stresses in Science and Technology*, V. Hauk and E. Macherauch, eds., DGM Informationsgesellschaft mbH, Oberursel, Federal Republic of Germany, 1987, pp. 493-500.
17. K.H. Jack: *Proc. R. Soc.*, 1948, vol. A195, pp. 34-55.
18. R. Delhez, E.J. Mittemeijer, Th.H. de Keijser, and H.C.F. Rozendaal: *J. Phys. E*, 1977, vol. 10, pp. 784-85.
19. M.A.J. Somers, N.M. van der Pers, D. Schalkoord, and E.J. Mittemeijer: *Metall. Trans. A*, 1989, vol. 20A, pp. 1533-39.
20. *International Tables for X-Ray Crystallography*, vol. III, Physical and Chemical Tables, The Kynoch Press, Birmingham, UK, 1968, pp. 162-65.
21. K. Salmutter and F. Stangler: *Z. Metallkd.*, 1969, vol. 51, pp. 544-48.
22. V. Hauk and H. Kockelmann: *Arch. Eisenhüttenwes.*, 1976, vol. 31, pp. 38-41.
23. F. Bollenrath, V. Hauk, and E.H. Müller: *Z. Metallkd.*, 1967, vol. 58, pp. 76-82.
24. Z. Przyłęcki and L. Małdziński: in *Proc. 4th Int. Conf. on Carbides, Nitrides, and Borides*, Technical Univerity, Poznań, Kołobrzeg, Poland, 1987, pp. 153-62.
25. U. Gösele and K.N. Tu: *J. Appl. Phys.*, 1982, vol. 53, pp. 3252-60.
26. H.C.F. Rozendaal, P.J. van der Schaaf, P.F. Colijn, and E.J. Mittemeijer: *Metall. Trans. A*, 1983, vol. 14A, pp. 395-99.
27. M.A.J. Somers, P.F. Colijn, and E.J. Mittemeijer: *Z. Metallkd.*, in press.
28. C. Wagner: in *Diffusion in Solids, Liquids and Gases*, W. Jost, Academic Press, London, 1960, p. 71.
29. B. Přenosil: *Härterei-Tech. Mitt.*, 1973, vol. 28, pp. 157-64.
30. E.J. Mittemeijer, M. van Rooijen, I. Wierzyłłowski, H.C.F. Rozendaal, and P.F. Colijn: *Z. Metallkd.*, 1983, vol. 74, pp. 473-87.
31. P.M. Hekker, H.C.F. Rozendaal, and E.J. Mittemeijer: *J. Mater. Sci.*, 1985, vol. 28, pp. 719-29.
32. P. Ferguson and K.H. Jack: *Heat Treatment '81*, The Metals Society, London, 1983, pp. 158-63.
33. Y.S. Touloukian, R.K. Kirby, R.E. Taylor, and P.D. Desai: *Thermal Expansion: Metallic Elements and Alloys*, IPI/Plenum, New York, NY, 1976, vol. 12.
34. R. Delhez, Th.H. de Keijser, E.J. Mittemeijer, B.J. Thijsse, M.A. Hollanders, O.B. Loopstra, and W.G. Sloof: *Aust. J. Phys.*, 1988, vol. 41, pp. 261-82.
35. M.A.J. Somers and E.J. Mittemeijer: *Metall. Trans. A*, in press.
36. M. Murakami: *J. Appl. Phys.*, 1982, vol. 53, pp. 3560-65.
37. M. Murakami, F.S. Kuan, and I.A. Blech: in *Treatise on Materials Science and Technology*, K.N. Tu and R. Rosenberg, eds., Academic Press, New York, NY, 1982, vol. 24, pp. 163-210.
38. W.G. Sloof, M.A.J. Somers, R. Delhez, and E.J. Mittemeijer: in *Proc. 2nd Int. Conf. on Residual Stresses*, G. Beck, S. Denis, and A. Simon, eds., Elsevier Applied Science, London, UK, 1989, pp. 304-09.